PHYSICAL REVIEW MATERIALS **1**, 054004 (2017)

Strain-induced band engineering in monolayer stanene on Sb(111)

Jian Gou,[1,3] Longjuan Kong,[1,3] Hui Li,[2] Qing Zhong,[1,3] Wenbin Li,[1,3] Peng Cheng,[1,3] Lan Chen,[1,3,*] and Kehui Wu[1,3,4,†]
[1]*Institute of Physics, Chinese Academy of Sciences, Beijing 100190, China*
[2]*Beijing Advanced Innovation Center for Soft Matter Science and Engineering,*
Beijing University of Chemical Technology, Beijing 100029, China
[3]*School of Physics, University of Chinese Academy of Sciences, Beijing 100049, China*
[4]*Collaborative Innovation Center of Quantum Matter, Beijing 100871, China*

(Received 26 May 2017; revised manuscript received 4 September 2017; published 24 October 2017)

The two-dimensional (2D) allotrope of tin with low buckled honeycomb structure named stanene is proposed to be an ideal 2D topological insulator with a nontrivial gap larger than 0.1 eV. Theoretical works also pointed out the topological property of stanene amenability to strain tuning. In this paper we report the successful realization of high quality, monolayer stanene film as well as monolayer stanene nanoribbons on Sb(111) surface by molecular-beam epitaxy, providing an ideal platform to the study of stanene. More importantly, we observed a continuous evolution of the electronic bands of stanene across the nanoribbon, related to the strain field gradient in stanene. Our work experimentally confirmed that strain is an effective method for band engineering in stanene, which is important for fundamental research and application of stanene.

DOI: 10.1103/PhysRevMaterials.1.054004

I. INTRODUCTION

Two-dimensional (2D) topological insulators (TIs) are featured by an energy gap in the interior and nontrivial, gapless states along the edge that can be described by the Dirac equation [1,2]. The expected helical spin-polarized transport makes 2D TIs promising materials that could serve as a platform for realizing quantum spin Hall (QSH) states [1,3], quantum computing [4], and spintronic device applications [5]. One 2D TI proposed by theorists is graphene [1], but the extremely small energy gap (about 10^{-3} meV) opened by spin-orbit coupling (SOC) makes it unlikely to observe any real effect in the experimental accessible temperature range [6]. In 2007, quantum spin Hall effect (QSHE) was observed in an HgTe quantum well [7]. However, fabrication of an HgTe quantum well is very difficult and successful experiment based on HgTe is very limited. Therefore, searching for a new 2D TI is desirable. Besides bismuth in group *V* of the periodic table [8,9], other group-*IV* elements in honeycomb structures, have been illustrated to possess the QSH state because of low-buckled geometry and larger SOC by theoretical calculations [10,11]. Especially single layer tin, namely stanene, was theoretically predicted an intrinsic SOC gap opening as large as 100 meV, suggesting the possibility of realizing the room-temperature QSH effect [12,13]. Moreover, by chemical functionalization of stanene, a parity exchange between occupied and unoccupied bands occurs at the Γ point and creates a nontrivial bulk gap of up to 0.3 eV [12]. Remarkably, such a large bulk gap is strongly associated with the in-plane strain induced by surface functionalization. Besides, other unique physics properties, such as enhanced thermoelectricity, topological superconductivity, giant magnetoresistance, and quantum anomalous Hall effects, have been proposed for stanene [14–17].

Considering the fact that stanene is one of the most promising, simplest 2D TI materials presently, it is very important to systematically investigate its structure and electronic properties, especially the possible effect of engineering its electron band structure under controllable strain [13,18,19]. Recently, the only experimental realization of stanene was reported on Bi_2Te_3, but the growth of tin on Bi_2Te_3 adopts a Vollmer-Weber growth mode (island growth) [20]. The difficulty in successful realization of stanene is because the two-dimensional material preparation largely depends on the substrate selection with proper substrate interaction. Different from silicene and germanene, which consist of semiconductor elements and can be synthesized on metal substrates [21–23], metal tin on ordinary metal surface prefers to form a surface alloy [24–28]. Looking for a proper semimetal or semiconductor substrate to realize uniform monolayer stanene will be the initial stage of experimental investigation on the strain effect on the electronic structures of stanene.

Here we report the successful growth of uniform monolayer stanene on Sb(111) surface by molecular beam epitaxy (MBE). Combined with scanning tunneling microscopy/spectroscopy (STM/STS) and first-principles calculations, we have revealed that monolayer stanene on Sb(111) has a compressed honeycomb lattice. Moreover, we have demonstrated a strain-induced electron band engineering effect in stanene nanoribbons. The electronic bands corresponding to $P_{x,y}^{+}$ orbitals of Sn move to Fermi level gradually along the transverse direction across the nanoribbon, which are proven to be a result of strain variation across the stanene ribbon. These results pave the way to future applications of stanene in electronic and spintronic devices.

Antimony is a layered semimetal with *ABC* staking sequence along the [111] crystallographic direction. Every biatomic Sb layer can be considered as buckled honeycomb lattice similar to stanene, and the interactions between layers similar to van der Waals interactions are weak. As a result, the Sb(111) surface can be easily obtained by cleavage [29,30]. More importantly, previous works on Sb/Sn binary alloy revealed a structure of intercalating pure Sb and Sn layers along the hexagonal *c* axis [31,32], suggesting that a layer-by-layer growth of Sn on Sb is possible.

---

[*] lchen@iphy.ac.cn
[†] khwu@iphy.ac.cn

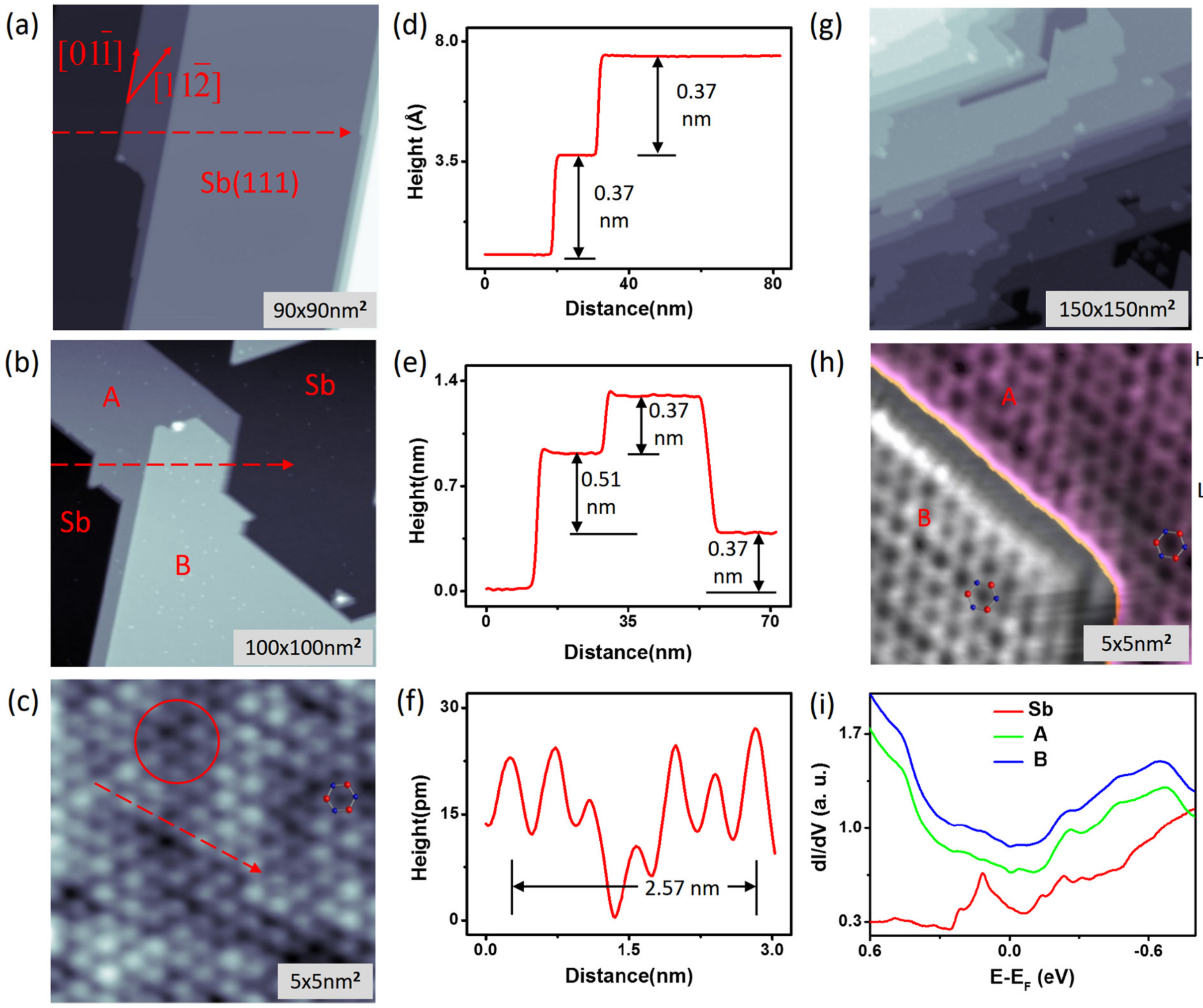

FIG. 1. Single Sn layer grown on Sb(111). (a) STM topographic image (−2.2 V, 90 pA) of clean Sb(111) surface with straight step edges. Crystallographic axes are labeled with red arrows. (b) STM topographic image (−2.0 V, 90 pA) of 0.5 ML tin grown on Sb(111). Tin terrace *A*, *B*, and substrate Sb are highlighted by corresponding letters. (c) High-resolution STM image of stanene (0.40 V, 100 pA). Depression area marked by red circle illustrates a clear honeycomblike atomic structure as illustrated by a ball-and-stick model nearby. (d)–(f) Height line profiles along the dashed arrows in (a)–(c), respectively. The step heights are indicated. (g) Large scale STM topographic image of stanene with a higher coverage (0.95 ML) (−2.4 V, 90 pA). (h) Visibility enhanced high-resolution STM image contains terrace *A* and *B* (0.4 V, 0.3 nA). Two ball-and-stick models are superimposed on the protrusions to indicate the atomic structure. (i) dI/dV spectra taken on a clean Sb(111) terrace (red), island *A* (green), and *B* (blue), respectively. The curves are offset vertically for clarity. All models keep the same definition as in Fig. 2(b).

II. PROCEDURES

The experiments were carried out in a home-built ultrahigh vacuum STM/MBE system. The single crystal Sb(111) surface was cleaned by a standard Ar^+ ion sputtering and annealing process. Sn with the purity of 99.999% was evaporated from a resistance-heating crucible. During the deposition, the Sb(111) substrate was kept at about 400 K in the MBE chamber with background pressure better than 2×10^{-10} Torr. After Sn deposition, the sample was transferred *in situ* to the STM chamber. All STM and STS measurements were performed at liquid-helium temperature by a chemically etched tungsten tip. The differential conductance (dI/dV) spectra were measured by the in-plane ac component in the tunneling current with a lock-in amplifier by superimposing an ac voltage (10 mV, 669 Hz) on the given dc tip bias relative to the sample. The STM topographic images were processed by WSxM [33].

First-principles density functional theory calculations were carried out with the Vienna *ab initio* Simulation Package (VASP) [34]. In the present calculations, the interaction between valence and core electrons was described by the projector-augmented wave (PAW) and the exchange-correlation interaction was treated using the generalized gradient approximation (GGA) in the formulation of the Perdew-Burke-Ernzerhof (PBE) function [35,36]. The plane-wave cutoff energy was set to 500 eV and the vacuum space was set to be ∼19 Å. A biatomic tin film was placed on a three-layer diatomic 1 × 1 Sb (111) slab (convergent number of layers) with fixed bottom layer to mimic the semi-infinite solid. The uppermost surface layers and stanene were fully relaxed until the residual force on each atom was less than 0.01 eV/Å.

III. RESULTS AND DISCUSSION

The typical STM image of Sb(111) surface is shown in Fig. 1(a), in which the crystallographic directions of Sb(111) can be determined by the straight steps. The line profile across the steps [Fig. 1(d)] reveals a step height of about 0.37 ± 0.01 nm, consistent with the thickness of single Sb layer. Figure 1(b) is an STM image of the Sb(111) surface after deposition of about 0.5 monolayer (ML) Sn. Sn islands with triangular and strip shapes are formed around the step edges of the Sb(111) substrate, and the edges of Sn islands are along the same high-symmetry crystallographic orientations of Sb(111). Another feature in Fig. 1(b) is that two different layers of Sn seem to be formed on the Sb(111) surface: the first layer (label *A*) and second layer (label *B*). But from the line profile across steps of Sb(111) and Sn islands [Fig. 1(e)], two different heights appear. The first Sn layer (*A*) has a height of 0.51 ± 0.01 nm relative to Sb substrate, while the height difference between *B* and *A* is 0.37 ± 0.01 nm, which is same as the height of a single Sb layer. Therefore, we believe island *B* is not a second Sn layer, but the same first Sn layer on a Sb terrace higher than that below island *A*. The similar phenomena can also be found in FeO/Pt(111) growth [37]. Moreover, the STS measurements on terraces of *A* and *B* reveal the same curve of local density of states (LDOS) [Fig. 1(i)], proving they are the same Sn layer.

The atomic structure of the first Sn layer is shown in the high-resolution STM image in Fig. 1(c), in which we found that the brightness of protrusions is inhomogeneous. In the depression area marked by the red circle a buckled honeycomb structure can be clearly revealed, suggesting that the Sn layer is a monolayer stanene structure. The line profile [Fig. 1(f)] along the red dashed arrow shown in Fig. 1(c) indicates a similar lattice constant (0.43 ± 0.01 nm) with substrate which is slightly smaller than either the Sn(111) surface [38] or freestanding stanene (0.468 nm) [12]. The smaller lattice constant suggests the existence of compressive strain in stanene on Sb(111), which may cause a slight fluctuation in the buckling degree of Sn atoms, and it explains the inhomogeneity in the image contrast in Fig. 1(c). Additionally, the high-resolution STM image containing both A and B terraces shown in Fig. 1(h) reveals the same honeycomb structures and identical crystallographic orientations, giving more evidence that both of them are monolayer stanene. Increasing tin coverage, a completed monolayer stanene can be formed on the entire substrate surface, as shown in Fig. 1(g). Further deposition of Sn atoms on Sb(111) with coverage exceeding one monolayer will form 2 × 2 reconstruction on the top of Sn layer [39], which is similar to the α-Sn(111) grown on InSb(111) substrate [38,40]. Therefore, the growth of tin on Sb(111) should be a layer-by-layer mode.

Next, we have determined the stacking configuration of stanene on Sb(111) substrate through a high-resolution STM image. Figure 2(a) gives an atomic-resolution image where the atoms on stanene and the Sb(111) substrate are resolved simultaneously, thus the relative position of the stanene lattice and the Sb(111) lattice can be determined. According to crystallographic orientation of Sb(111) [Fig. 1(a)], a ball-and-stick model of the Sb(111) surface is superimposed and extends from Sb to stanene (bottom right) to illustrate the stacking relationship. Unambiguously, the stacking relationship between stanene and the Sb(111) surface is determined to be a AA' stacking sequence, in which the lower bucked Sn atoms locate at the topmost site of Sb and upper bucked Sn atoms locate at the sites above the second layer Sb atoms. The AA' stacking sequence in stanene on Sb(111) is different than the germanene on Sb(111), which adopts an *AB* stacking configuration [41]. The structural model of stanene on Sb(111) is shown in Fig. 2(b).

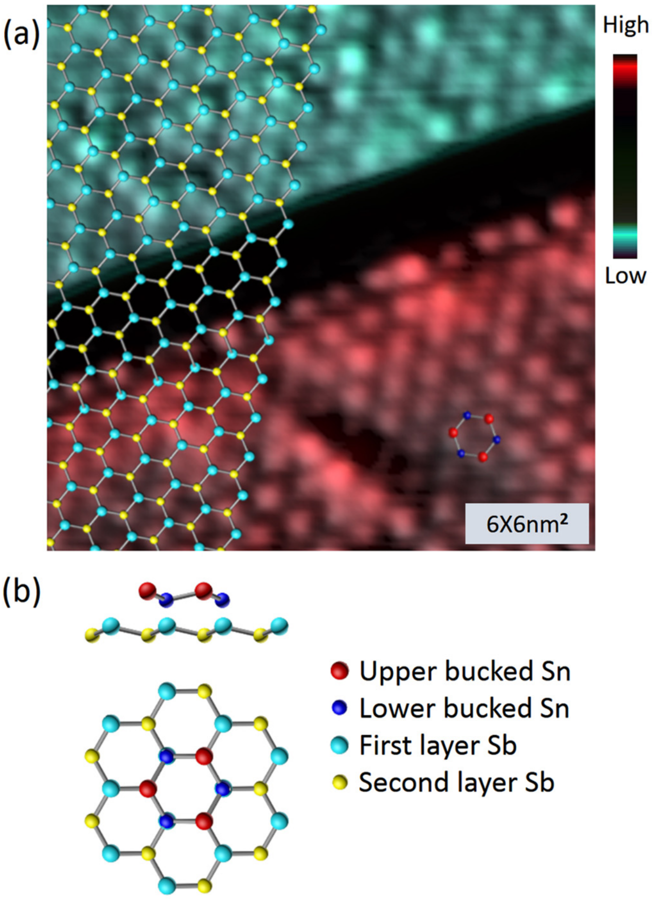

FIG. 2. Atomic structure and staking mode of stanene on Sb(111). (a) Atomic-resolution STM image of stanene (red, lower part) on Sb(111) substrate (green, upper part) (0.4 V, 0.3 nA). Visibility of image is enhanced on the premise that there is no relative shifting between all the protrusions. A honeycomb model is superimposed on image and extended from Sb to stanene to illustrate the staking relationship between them. (b) Top view (upper panel) and side view (middle panel) of the stacking model for stanene on Sb(111). The atom definition with different colors is shown in the bottom panel.

The stacking configuration of stanene adlayer on Sb(111) is reconfirmed by first-principles calculations on infinite stanene monolayer adsorbed on Sb(111). The calculation results indicate that AA' stacking is an energy favorable structure for stanene on Sb(111). Based on such a compressed honeycomb stanene layer with AA' stacking on Sb(111), the calculated electronic structure is plotted in Fig. 3(a). The total electronic bands of stanene/Sb(111) with SOC and the projected bands on

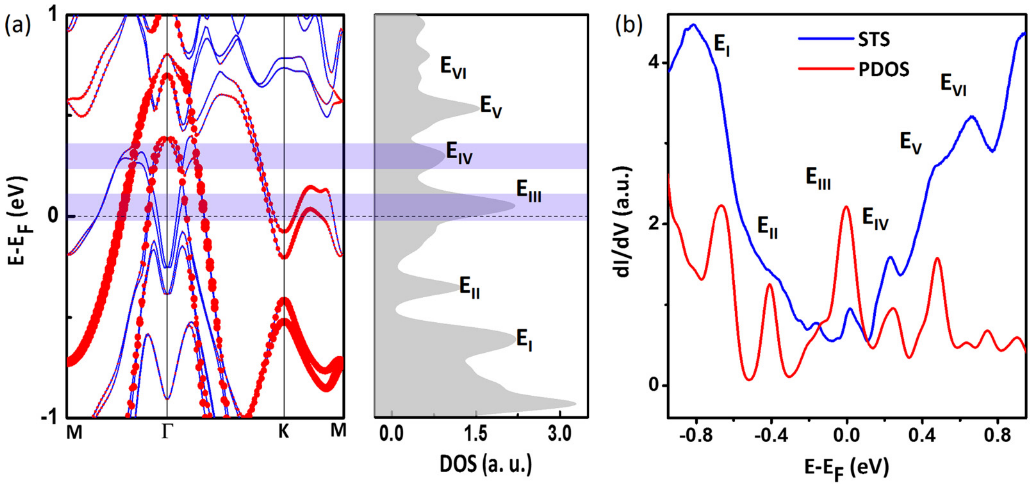

FIG. 3. Electronic structure of stanene on Sb(111). (a) Left panel: calculated band structure with SOC. Blue curves stand for the total band structure including three layers of biatomic Sb(111) substrate and a single layer stanene on it. Red dots indicate the projected bands on stanene and the size of dots represents the weights factor. Right panel: calculated DOS of stanene. (b) Comparison of experimental dI/dV spectra (blue) and calculated DOS (red) of stanene on Sb(111). Energy positions of all the calculated DOS maxima agree with peaks in the experimental data very well. Several featured DOS maxima are labeled with $E_i (i = \text{I, II, III, IV, V, VI})$.

stanene adlayer are shown in the left panel. Remarkably, a gap of ~200 meV is opened at the K point, which is about twice that in freestanding stanene. This demonstrates the significant effect of the compressive strain in stanene on Sb(111) (−8% lattice constant change relative to the freestanding form). Meanwhile, the electronic band consisting of $P^+_{x,y}$ orbitals of tin atoms near the Γ point cross over the Fermi level and make stanene metallic, which is similar to that in stanene/Bi$_2$Te$_3$ [20].

The corresponding DOS of stanene is shown in the right part of Fig. 3(a), and the DOS maxima are labeled with $E_i (i = \text{I, II, III, IV, V, VI})$ for identification. Compared with the band structure, the E_{IV} and E_{III} peaks can mainly be attributed to the Van Hove singularities of the $P^+_{x,y}$ band at the Γ point, and the flat bands at K-M, respectively. In other words, these two peaks are pure bands of stanene. On the contrary, other peaks are mainly contributed by the hybridized Sn orbitals with underlying Sb atoms, except for E_{V} which is contributed by $P^+_{x,y}$ band partly. The comparison of the calculated DOS and experimental STS curve is shown in Fig. 3(b). We found that the peaks in the STS curve correspond to the DOS maxima very well, except for a slight energy shift of less than 50 meV. The perfect matching between calculated DOS and STS measurements strongly supports our structural model for monolayer stanene on Sb(111). On the other hand, the slight energy shift may result from n-type doping which comes from surface defects. A similar doping effect was also found in other 2D materials with honeycomb structures [42,43].

Since the growth of stanene islands starts from the step edges of the Sb(111) surface, we can obtain stanene nanoribbons on the Sb(111) surface with narrow terrace arrays, as shown in Fig. 4(a). We performed STS measurements on a stanene nanoribbon shown in Fig. 4(b) along the transverse direction across the nanoribbon. As illustrated in Figs. 4(d) and 4(f), a set of dI/dV spectra were depicted as a function of distance along the highest crystallographic orientation indicated by the black arrow in Fig. 4(b). From the outer side to the inner side, apart from the apparent inhomogeneity of STS intensity which comes from the localized strain fluctuation as discussed in Fig. 1(c), one can explicitly see an E'_{V} peak split from E_{V}, and the positions of E_{III} and E_{IV} peaks move to Fermi level independently. On the contrary, other peaks are kept unchanged. The same phenomenon is also found on other nanoribbons [39].

As we mentioned before, the E_{III} and E_{IV} peaks are pure bands of stanene. These bands are derived from the $P^+_{x,y}$ orbitals of tin, which are sensitive to in-plane strain according to previous theoretical works [12]. On the other hand, based on the stacking configuration of stanene on Sb(111), and the STM observation that the edges of stanene nanoribbons are along the crystallographic orientation of Sb(111) [Fig. 4(b)], we can conclude that the edges of nanoribbons are zigzaglike. Due to the buckled structure of stanene, there are two kinds of zigzag edges: type A (outermost atoms are upper buckled) and type B (outermost atoms are lower buckled), shown in Fig. 4(c). The stanene nanoribbon interacts with the Sb(111) substrate mainly through its edge atoms as these atoms have unsaturated dangling bonds. The type-A edge should have a weaker interaction with Sb(111) substrate compared with the type-B edge, because the upper buckled tin atoms have further distance from substrate. In consequence, the compressive strain at the outer edge is relatively small and will increase gradually to the inner side along the transverse direction.

The evolution of E_{III} and E_{IV} peaks from the outer to the inner edge of a stanene nanoribbon proves that the band structure of stanene can be tuned by strain. This is remarkable as further band engineering, such as band crossing or nontrivial gap opening, may be achieved [12]. Considering the E_{V} peak partly consisting of $P^+_{x,y}$ orbitals at the Γ point [Fig. 3(a)], which are sensitive to in-plane strain, the evolution of strain also induces electronic bands corresponding to $P^+_{x,y}$ orbitals in the E_{V} peak moving to Fermi level, which results in a E'_{V} peak splitting from the E_{V} peak and movement. The previous

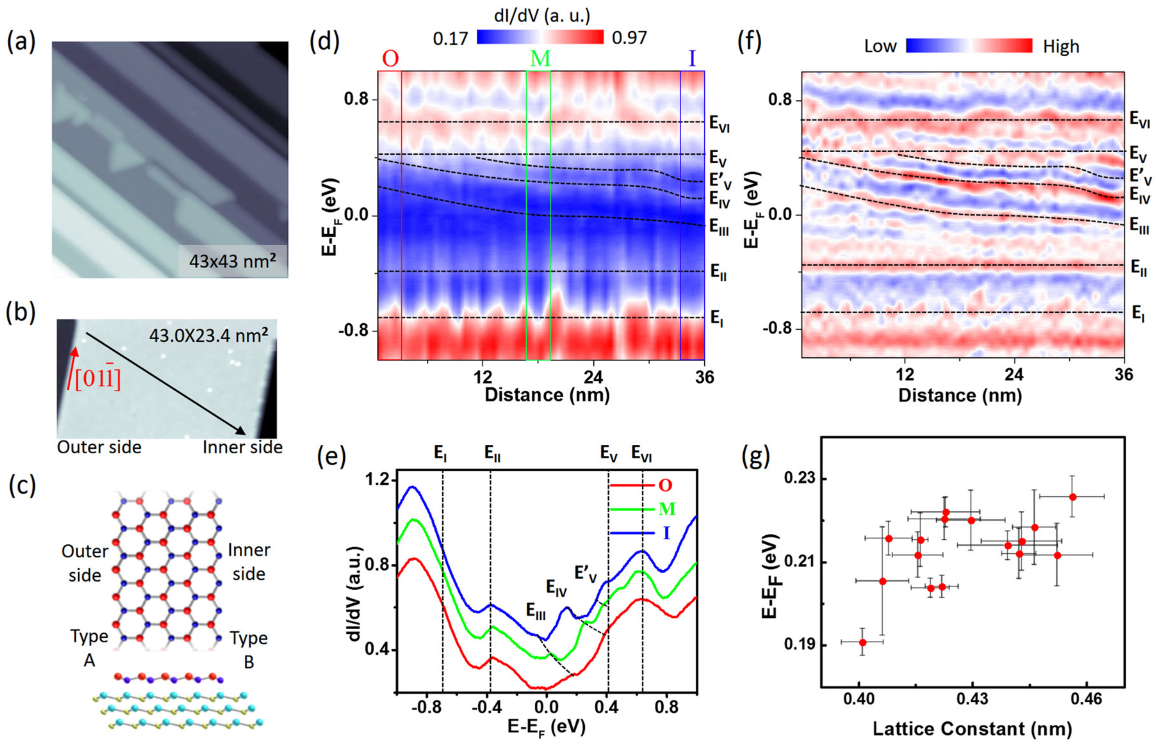

FIG. 4. Strain-induced bands engineering. (a) STM topographic image of stanene nanoribbon on narrow substrate terraces (−1.5 V, 90 pA). (b) STM image of a stanene nanoribbon (−1.0 V, 87 pA). The crystallographic orientation of Sb(111) are labeled with red arrow. (c) Schematic atomic structure of stanene nanoribbon on Sb(111). Upper panel: top view (only stanene was shown). Lower panel: side view. (d) Color map of dI/dV spectra obtained along the line indicated by the black arrow in (c). (e) Average of the dI/dV spectra in rectangles labeled by the same colored O, M, I in (d), respectively. The curves are offset vertically for clarity. (f) Contour plot of second derivative of dI/dV spectra map in (d). Dashed lines marked by $E_i (i = \mathrm{I, II, III, IV, V, VI})$ in (d)–(f) are added along the featured STS peaks to guide the eye. (g) Statistics of the energy position dependence of E_{III} on lattice constant of stanene.

theoretical work suggests that the $P^{+}_{x,y}$ orbitals split at the Γ point due to the SOC effect for Sn-Sn bonds, which correspond to the E_{IV} and E'_{V} peaks in our experiments. The interval between the splitting $P^{+}_{x,y}$ orbitals can be slightly enlarged under hydrostatic strain, which accorded with the unchanged interval between E_{IV} and E'_{V} [Figs. 4(d) and 4(f)] from the outer side to the inner side very well, proving existence of the strain-induced band engineering.

Meanwhile, the strain-induced band tuning effect can also be revealed in larger stanene islands. For example, we performed STS measurements at various sites on the terrace of stanene islands with fluctuation of buckling degree of Sn atoms like in Fig. 1(c). The energy position of the E_{III} peak in dI/dV spectra shows an obvious monotonous dependence on the measured local lattice constant, as shown in Fig. 4(g). As the local lattice constant is directly related with the in-plane stain, this once again verifies the strain-induced band engineering effect in stanene.

IV. SUMMARY

Although free-standing stanene is a large gap 2D TI, stanene on different substrates, such as Bi_2Te_3 [20], so far all suffer from the interaction between stanene and the substrate, and become topological trivial systems [44]. It is therefore crucial to restore its band crossing and topological nature, for example by strain engineering, in order to enable different applications. Stanene on Sb(111) provides an ideal stanene system, as monolayer stanene can be uniformly fabricated on a large scale. The effective band engineering by varying in-plane strains implies that this is a promising way. As antimony is a layered material that can be exfoliated vastly, growing stanene on ultrathin antimony film and combined with halogenations adsorption may further enhance the strain engineering effect, and even realize a nontrivial gap opening in stanene. Finally, single layer antimony, namely antimonene, is semiconducting, whose structure is easy to tune [45,46]. Combing stanene/antimonene offers a clean, interesting van der Waals heterostructure system, whose properties are worth further investigation [47].

ACKNOWLEDGMENTS

We thank Dr. Y. Xu of Tsinghua University for constructive discussion. This work was supported by the MOST of China (Grants No. 2016YFA0300904, No. 2016YFA0202301, No. 2013CBA01601, and No. 2013CB921702), the NSF of China (Grants No. 11674366, No. 11674368, No. 11334011, and No. 11304368), and the Strategic Priority Research Program of the Chinese Academy of Sciences (Grant No. XDB07020100).

[1] C. L. Kane and E. J. Mele, Phys. Rev. Lett. **95**, 226801 (2005).
[2] B. A. Bernevig, T. L. Hughes, and S.-C. Zhang, Science **314**, 1757 (2006).
[3] X.-L. Qi and S.-C. Zhang, Phys. Today **63**(1), 33 (2010).
[4] C. Nayak, S. H. Simon, A. Stern, M. Freedman, and S. Das Sarma, Rev. Mod. Phys. **80**, 1083 (2008).
[5] D. Pesin and A. H. MacDonald, Nat. Mater. **11**, 409 (2012).
[6] Y. Yao, F. Ye, X.-L. Qi, S.-C. Zhang, and Z. Fang, Phys. Rev. B **75**, 041401 (2007).
[7] M. König, S. Wiedmann, C. Brüne, A. Roth, H. Buhmann, L. W. Molenkamp, X.-L. Qi, and S.-C. Zhang, Science **318**, 766 (2007).
[8] M. Wada, S. Murakami, F. Freimuth, and G. Bihlmayer, Phys. Rev. B **83**, 121310 (2011).
[9] F. Reis, G. Li, L. Dudy, M. Bauernfeind, S. Glass, W. Hanke, R. Thomale, J. Schäfer, and R. Claessen, Science **357**, 287 (2017).
[10] C.-C. Liu, W. Feng, and Y. Yao, Phys. Rev. Lett. **107**, 076802 (2011).
[11] T. Amlaki, M. Bokdam, and P. J. Kelly, Phys. Rev. Lett. **116**, 256805 (2016).
[12] Y. Xu, B. Yan, H. J. Zhang, J. Wang, G. Xu, P. Tang, W. Duan, and S. C. Zhang, Phys. Rev. Lett. **111**, 136804 (2013).
[13] B. v. d. Broek, M. Houssa, E. Scalise, G. Pourtois, V. V. Afanas‘ev, and A. Stesmans, 2D Mater. **1**, 021004 (2014).
[14] Y. Xu, Z. Gan, and S. C. Zhang, Phys. Rev. Lett. **112**, 226801 (2014).
[15] J. Wang, Y. Xu, and S.-C. Zhang, Phys. Rev. B **90**, 054503 (2014).
[16] S. Rachel and M. Ezawa, Phys. Rev. B **89**, 195303 (2014).
[17] S. C. Wu, G. Shan, and B. Yan, Phys. Rev. Lett. **113**, 256401 (2014).
[18] Y. Xu, P. Tang, and S.-C. Zhang, Phys. Rev. B **92**, 081112 (2015).
[19] P. Lu, L. Wu, C. Yang, D. Liang, R. Quhe, P. Guan, and S. Wang, Sci. Rep. **7**, 3912 (2017).
[20] F. F. Zhu, W. J. Chen, Y. Xu, C. L. Gao, D. D. Guan, C. H. Liu, D. Qian, S. C. Zhang, and J. F. Jia, Nat. Mater. **14**, 1020 (2015).
[21] P. Vogt, P. De Padova, C. Quaresima, J. Avila, E. Frantzeskakis, M. C. Asensio, A. Resta, B. Ealet, and G. Le Lay, Phys. Rev. Lett. **108**, 155501 (2012).
[22] L. Meng, Y. Wang, L. Zhang, S. Du, R. Wu, L. Li, Y. Zhang, G. Li, H. Zhou, W. A. Hofer *et al.*, Nano Lett. **13**, 685 (2013).
[23] M. Derivaz, D. Dentel, R. Stephan, M. C. Hanf, A. Mehdaoui, P. Sonnet, and C. Pirri, Nano Lett. **15**, 2510 (2015).
[24] J. R. Osiecki and R. I. G. Uhrberg, Phys. Rev. B **87**, 075441 (2013).
[25] M. G. Barthès and C. Pariset, Thin Solid Films **77**, 305 (1981).
[26] M. T. Paffett and R. G. Windham, Surf. Sci. **208**, 34 (1989).
[27] A. K. Schmid, N. C. Bartelt, and R. Q. Hwang, Science **290**, 1561 (2000).
[28] Y. Guo, F. Pan, M. Ye, Y. Wang, Y. Pan, X. Zhang, J. Li, H. Zhang, and J. Lu, 2D Mater. **3**, 035020 (2016).
[29] B. Stegemann, C. Ritter, B. Kaiser, and K. Rademann, Phys. Rev. B **69**, 155432 (2004).
[30] J. Seo, P. Roushan, H. Beidenkopf, Y. S. Hor, R. J. Cava, and A. Yazdani, Nature (London) **466**, 343 (2010).
[31] V. Vassiliev, M. Lelaurain, and J. Hertz, J. Alloy. Compd. **247**, 223 (1997).
[32] L. Norén, R. L. Withers, S. Schmid, F. J. Brink, and V. Ting, J. Solid. State Chem. **179**, 404 (2006).
[33] I. Horcas, R. Fernandez, J. M. Gomez-Rodriguez, J. Colchero, J. Gomez-Herrero, and A. M. Baro, Rev. Sci. Instrum. **78**, 013705 (2007).
[34] G. Kresse and J. Furthmüller, Phys. Rev. B: Condens. Matter. **54**, 11169 (1996).
[35] J. P. Perdew, K. Burke, and M. Ernzerhof, Phys. Rev. Lett. **77**, 3865 (1996).
[36] P. E. Blöchl, Phys. Rev. B **50**, 17953 (1994).
[37] W. Weiss and M. Ritter, Phys. Rev. B **59**, 5201 (1999).
[38] T. Osaka, H. Omi, K. Yamamoto, and A. Ohtake, Phys. Rev. B **50**, 7567 (1994).
[39] See Supplemental Material at http://link.aps.org/supplemental/10.1103/PhysRevMaterials.1.054004 for the growth of Sn on Sb(111) with coverage exceeding 1BL, and two other examples of stain-induced band engineering on stanene nanoribbons.
[40] T. Eguchi, J. Nakamura, and T. Osaka, J. Phys. Soc. Jpn. **67**, 381 (1998).
[41] J. Gou, Q. Zhong, S. Sheng, W. Li, P. Cheng, H. Li, L. Chen, and K. Wu, 2D Mater. **3**, 045005 (2016).
[42] L. Zhang, P. Bampoulis, A. N. Rudenko, Q. Yao, A. van Houselt, B. Poelsema, M. I. Katsnelson, and H. J. W. Zandvliet, Phys. Rev. Lett. **116**, 256804 (2016).
[43] S. Jung, G. M. Rutter, N. N. Klimov, D. B. Newell, I. Calizo, A. R. Hight-Walker, N. B. Zhitenev, and J. A. Stroscio, Nat. Phys. **7**, 245 (2011).
[44] At least, we did not find any obviously conductive edge states at the outer zigzag side.
[45] X. Wu *et al.*, Adv. Mater. **29**, 1605407 (2017).
[46] M. Zhao, X. Zhang, and L. Li, Sci. Rep. **5**, 16108 (2015).
[47] A. K. Geim and I. V. Grigorieva, Nature (London) **499**, 419 (2013).